

Comparison of structural and optical properties of blue emitting $\text{In}_{0.15}\text{Ga}_{0.85}\text{N}/\text{GaN}$ multi-quantum-well layers grown on sapphire and silicon substrates

Cite as: AIP Advances 9, 025306 (2019); doi: 10.1063/1.5078743

Submitted: 28 October 2018 • Accepted: 30 January 2019 •

Published Online: 13 February 2019



Richard Liu,^{1,2}  Callan McCormick,^{1,2}  and Can Bayram^{1,2,a)} 

AFFILIATIONS

¹Department of Electrical and Computer Engineering, University of Illinois at Urbana-Champaign, Urbana, Illinois 61801, USA

²Micro and Nanotechnology Laboratory, University of Illinois at Urbana-Champaign, Urbana, Illinois 61801, USA

^{a)}Innovative COmpound semiconductoR LABoratory (ICORLAB); Email: cbayram@illinois.edu; Webpage: <https://icorlab.ece.illinois.edu>; Phone: +1 (217) 300-0978; Fax: +1 (217) 244-6375

ABSTRACT

Six periods of 2-nm-thick $\text{In}_{0.15}\text{Ga}_{0.85}\text{N}/13\text{-nm-thick GaN}$ blue emitting multi-quantum-well (MQW) layers are grown on sapphire (Al_2O_3) and silicon (Si) substrates. X-ray diffraction, Raman spectroscopy, atomic force microscopy, temperature-dependent photoluminescence (PL), Micro-PL, and time-resolved PL are used to compare the structural and optical properties, and the carrier dynamics of the blue emitting active layers grown on Al_2O_3 and Si substrates. Indium clustering in the MQW layers is observed to be more pronounced on Al_2O_3 than those on Si as revealed through investigating band-filling effects of emission centers, S-shaped peak emission energy shifts with increasing temperature, and PL intensity-peak energy spatial nonuniformity correlations. The smaller indium clustering effects in MQW on Si are attributed to the residual tensile strain in the GaN buffer layer, which decreases the compressive strain and thus the piezoelectric polarization field in the InGaN quantum wells. Despite a 30% thinner total epitaxial thickness of $3.3\text{ }\mu\text{m}$, MQW on Si exhibits a higher IQE than those on Al_2O_3 in terms of internal quantum efficiency (IQE) at temperatures below 250 K, and a similar IQE at 300 K (30% vs 33%). These results show that growth of blue emitting MQW layers on Si is a promising approach compared to those conventionally grown on Al_2O_3 .

© 2019 Author(s). All article content, except where otherwise noted, is licensed under a Creative Commons Attribution (CC BY) license (<http://creativecommons.org/licenses/by/4.0/>). <https://doi.org/10.1063/1.5078743>

I. INTRODUCTION

Indium gallium nitride (InGaN)/gallium nitride (GaN) multiple quantum well (MQW)-based blue light emitting diodes (LEDs) and their white LED derivatives have transformed the lighting industry thanks to their superior power efficiency, longevity, and compactness. The lack of commercially viable native GaN substrates necessitates InGaN/GaN LEDs to be grown on foreign substrates such as sapphire (Al_2O_3).¹ LEDs can also be grown on Si(111) substrates, which are widely available in very high quality and wafer sizes as

large as 450 mm at lower than one-fifth of the price per unit area. In the latter, the absorptive silicon substrate can then be removed after a flip-chip bonding scheme is employed. This approach can significantly reduce the cost and increase the market penetration of LED.² In addition, recent advances in III-nitrides growth on silicon have mitigated the thermal expansion and lattice mismatch issues with the use of stress management layers such as AlN buffer layers and SiN interlayers.³⁻⁵ Recent studies on electrically-injected and packaged LEDs showed instances where LED on Si outperforms those on Al_2O_3 .^{6,7} However, such studies have not been done for

LEDs on Al_2O_3 and Si substrates with identical blue emitting MQWs, inhibiting direct comparison of structural and optical properties of the blue emitting MQWs.

In this work, identical blue-emitting MQW layers without p-GaN caps are grown on c-plane Al_2O_3 (MQW- Al_2O_3) and Si(111) (MQW-Si) substrates. Structural studies using X-ray diffraction (XRD), Raman spectroscopy, and atomic force microscopy (AFM), and optical studies using Microphotoluminescence (μPL), temperature-dependent PL (TDPL), time-resolved PL (TRPL) are carried out in order to compare the structural and optical properties of MQWs on Al_2O_3 and Si substrates.

II. EXPERIMENTS AND DATA ANALYSIS

Figure 1 illustrates the cross section of (a) MQW- Al_2O_3 and (b) MQW-Si grown by metalorganic chemical vapor deposition (MOCVD). The blue-emitting active layers on the surface of both samples consist of six periods of 2-nm thick $\text{In}_{0.15}\text{Ga}_{0.85}\text{N}$ /13-nm thick GaN well-barrier pairs. The overall thickness of the epitaxial layers of MQW-Si ($3.3\ \mu\text{m}$) is thinner than that of MQW- Al_2O_3 ($4.6\ \mu\text{m}$). No cracks are observed on the surface of either samples.

Figure 2 shows the $200\ \mu\text{m} \times 200\ \mu\text{m}$ μPL mapping of (a) MQW- Al_2O_3 and (b) MQW-Si with the top row showing the MQW emission intensity variation and the bottom row showing the peak emission energy variation relative to their

respective averages using a continuous wave HeCd 325 nm laser. MQW- Al_2O_3 and MQW-Si exhibit integrated intensity uniformities of 5.1% and 4.1%, and average peak emission energies of $2.791\ \text{eV} \pm 3.7\ \text{meV}$ (444 nm) and $2.823\ \text{eV} \pm 1.4\ \text{meV}$ (439 nm), respectively. One noteworthy observation is that the strongly blue-shifted regions of MQW- Al_2O_3 coincide accurately with the high PL intensity regions, and conversely the red-shifted clusters overlap with the low PL intensity spots. Closer inspection of the spectra of these locations shows that the brighter regions emit additional photons only in the high energy shoulder when compared to the dimmer regions. This is attributed to the screening of the quantum confined stark effect (QCSE) and filling of the states in the emission centers.^{8,9} The lack of such observation in MQW-Si suggests the local energy minima are not as pronounced. Such local energy minima have been reported in the literature as a manifestation of indium clustering. To further explore the differences between the samples, surface analysis using atomic force microscopy (AFM) is conducted.

Figure 3 shows $20\ \mu\text{m} \times 20\ \mu\text{m}$ AFM scans of (a) MQW- Al_2O_3 and (b) MQW-Si with identical height scales. The surface morphology of MQW- Al_2O_3 shows a surface with step-flow terraces that have step heights of $\sim 0.3\ \text{nm}$, which corresponds to a monolayer of GaN. The threading dislocations in Fig. 3a has a density of $\sim 2.87 \times 10^8\ \text{cm}^{-2}$. The root-mean-square (RMS) surface roughness is measured as 1.17 nm. The surface of MQW-Si shows a different surface morphology that is covered by hexagonal spiral hillocks with a mixed type dislocation in the center that are $\sim 5\ \mu\text{m}$ apart and with a density of $6.56 \times 10^6\ \text{cm}^{-2}$.¹⁰ The threading dislocation of MQW-Si has a density of $\sim 3.20 \times 10^8\ \text{cm}^{-2}$. The long-range order of these hillocks is reflected in the high RMS roughness of 2.81 nm. To further explore the differences between the crystals structural analysis using X-ray diffraction (XRD) and Raman spectroscopy are carried out.

Figure 4 shows the (a) symmetric $\omega/2\theta$ XRD spectra and (b) Raman spectroscopy of the MQW- Al_2O_3 (blue, solid line) and on Si (red, dashed line). In Fig. 4a, the (004) GaN reflections are observed at $\theta \approx 73^\circ$ with InGaN/GaN MQW fringe peaks on the left for both samples and AlGaN buffer layers' peaks on the right for MQW-Si. The 0^{th} peak position of InGaN implies an average indium composition of $\sim 2\%$ across the MQW. The thickness of each well-barrier period is calculated from the fringe spacing using the relationship:¹¹

$$T = \frac{(n_i - n_j)\lambda}{2(\sin \theta_i - \sin \theta_j)}, \quad (1)$$

where n_i and n_j are the order of the i^{th} and j^{th} fringe peaks, respectively, and λ is the wavelength of the X-ray (Cu- $K_{\alpha 1}$, 0.154056 nm). This yields a well-barrier pair thickness of 14.8 nm. Asymmetric scan on the (102) reflection is conducted to evaluate composition of the $\text{Al}_{1-x}\text{Ga}_x\text{N}$ buffer layers. The lattice constants, a and c , are calculated using the d-plane spacing (d_{hkl}), which is the interplanar spacing of the lattice plane (hkl) that satisfy Bragg's condition:

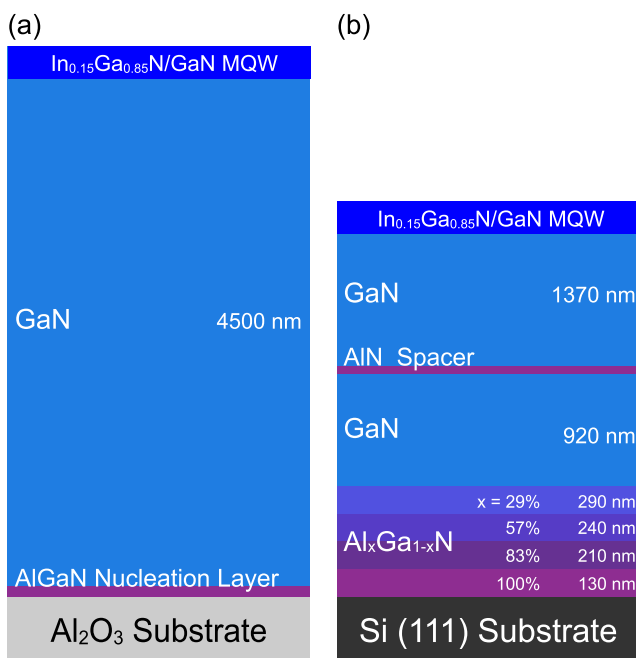


FIG. 1. Cross-sectional illustration of the MOCVD-grown (a) MQW- Al_2O_3 , and (b) MQW-Si. The MQW- Al_2O_3 is a $4.6\ \mu\text{m}$ -thick GaN on Al_2O_3 substrate with a thin AlN nucleation layer. The MQW-Si uses multiple AlGaN buffer layers with decreasing Al-composition and a thin AlN spacer in the GaN layer with an overall epitaxial thickness of $3.3\ \mu\text{m}$. Identical blue-emitting MQW layers are grown on both samples.

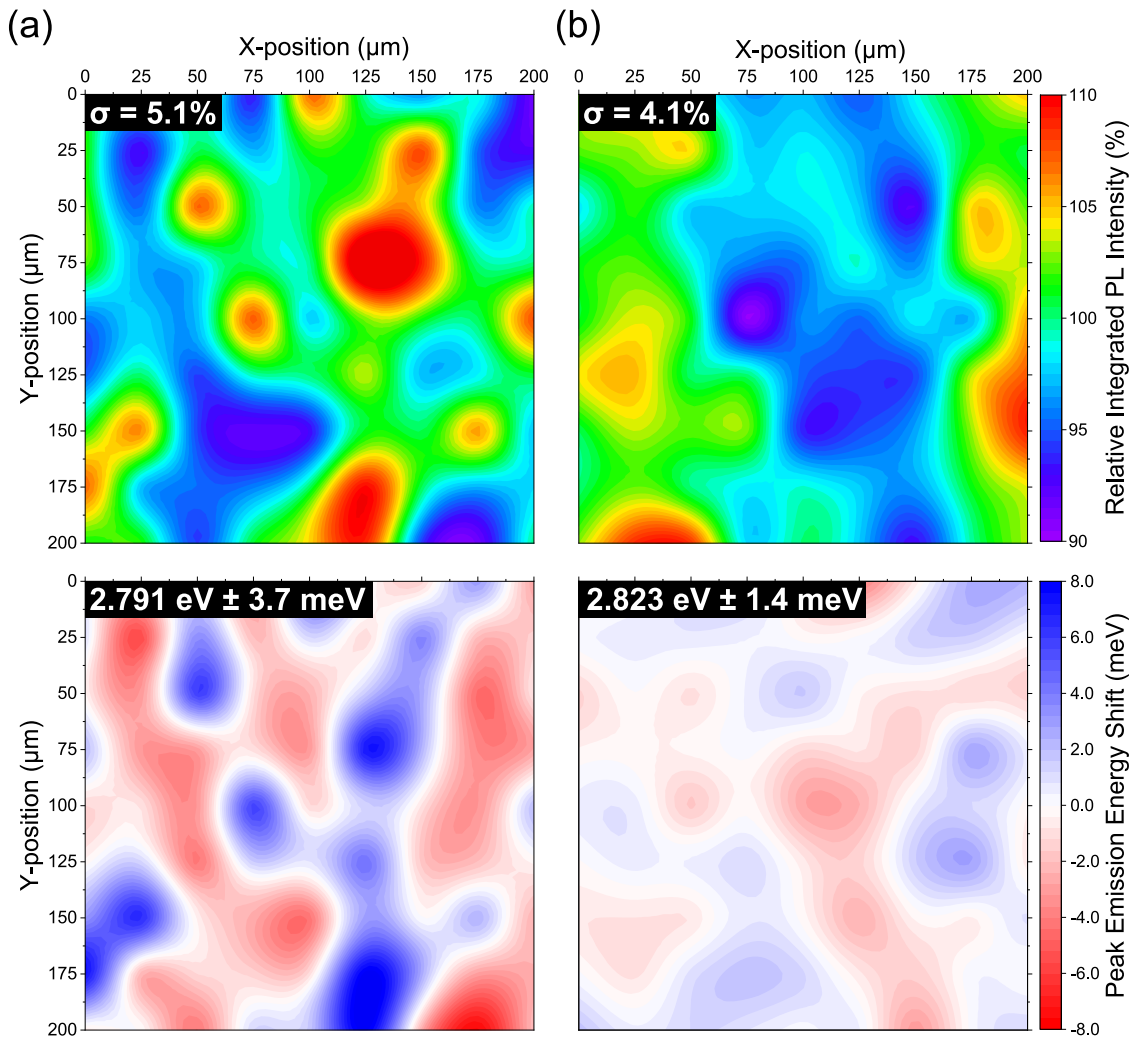


FIG. 2. Micro-photoluminescence mapping of (a) MQW-Al₂O₃ and (b) MQW-Si. The relative intensity is shown in the top row and peak emission energy in bottom row. MQW-Al₂O₃ exhibits a correlation between the intensity and the peak emission energy mapping with the high intensity locations showing a blue shift and vice versa.

$$\left(\frac{1}{d_{hkl}}\right)^2 = \frac{4}{3} \left(\frac{h^2 + hk + k^2}{a^2} \right) + \frac{l^2}{c^2} \quad (2)$$

and Poisson-Vegard's law:

$$\begin{aligned} \frac{c_m(x) - c_0(x)}{c_0(x)} &= -\frac{2\nu(x)}{1 - \nu(x)} \times \frac{a_m(x) - a_0(x)}{a_0(x)} \\ c_0(x) &= (1 - x)c_{\text{GaN}} + xc_{\text{AlN}} + \delta_c x(1 - x) \\ a_0(x) &= (1 - x)a_{\text{GaN}} + xa_{\text{AlN}} + \delta_a x(1 - x) \\ \nu(x) &= (1 - x)\nu_{\text{GaN}} + x\nu_{\text{AlN}} \end{aligned} \quad (3)$$

where $c_m(x)$ and $a_m(x)$ are the measured lattice constants, $c_0(x)$ and $a_0(x)$ are the relaxed lattice constants, $\nu(x)$ is the Poisson's ratio, δ_a and δ_c are the lattice bowing parameters.^{12,13} The compositions of the Al_{1-x}Ga_xN buffer layers are calculated in the order from the substrate to the surface to be

1.00, 0.83, 0.57, and 0.29. Additionally, the lattice constants and strain of the GaN layers are also calculated and tabulated in Table I. The XRD shows the GaN layers of MQW-Al₂O₃ and MQW-Si are under compressive (-0.17%) and tensile (0.19%), respectively.

The ω scan of the GaN peak of (002) and (102) reflections are used to quantify the defectivity of the GaN material. The densities of screw- and edge-type dislocations are related to the ω scan FWHM of the (002) plane (β_{002}) and the (102) plane (β_{102}) through the Burgers vector lengths of the edge type dislocation ($b_{\text{edge}} = 0.3189$ nm), and of the screw type dislocation ($b_{\text{screw}} = 0.5185$ nm) using the following relations:¹¹

$$D_{\text{screw}} = \frac{\beta_{(002)}^2}{4.35 \times b_{\text{screw}}^2} \quad (4)$$

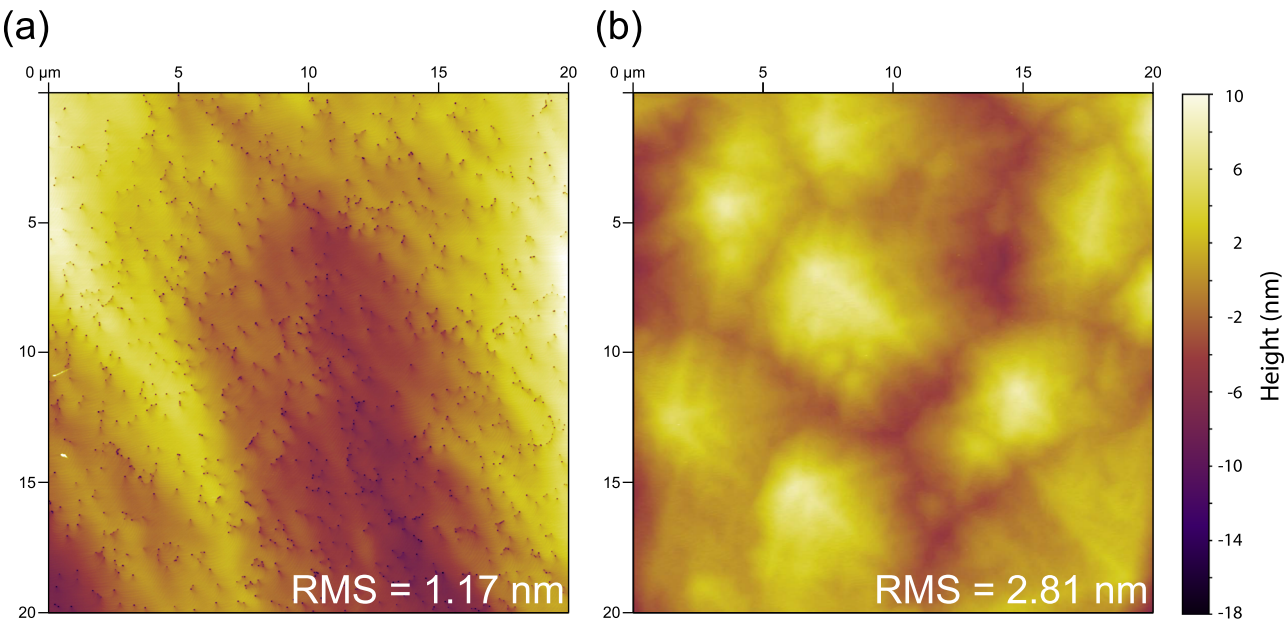


FIG. 3. Large scale $20 \times 20 \mu\text{m}^2$ AFM scans of (a) MQW- Al_2O_3 and (b) MQW-Si. The surface of MQW- Al_2O_3 shows step-flow terraces, whereas the surface of MQW-Si is populated with hillocks.

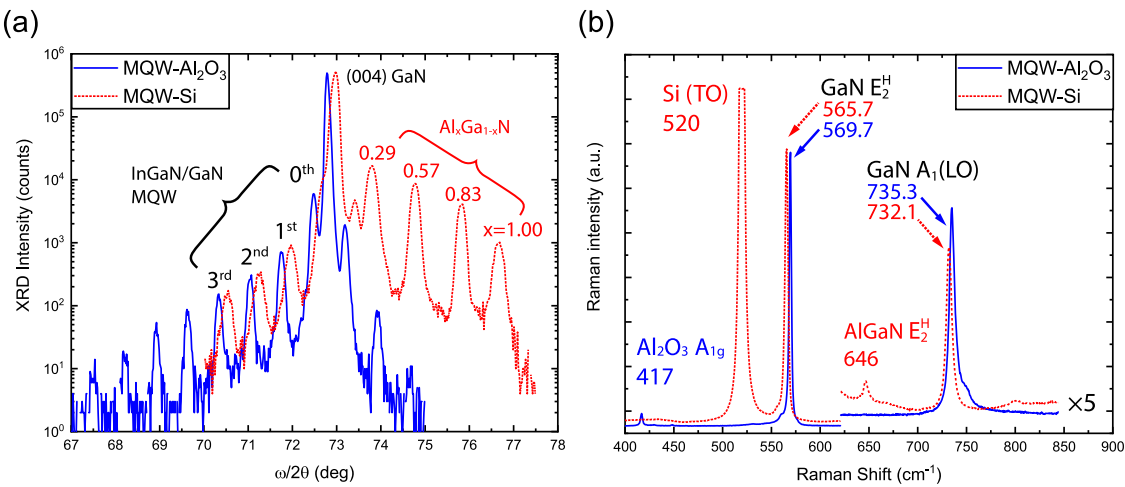


FIG. 4. (a) symmetric $\omega/2\theta$ XRD showing the (004) reflections from AlGaIn buffer layers, GaN, and InGaN MQWs. GaN peak in MQW-Si exhibits a broader FWHM (732 vs 460 arcsec) than MQW- Al_2O_3 . (b) Raman spectroscopy shows a blue shift in both the E_2^H and $A_1(\text{LO})$ peaks of GaN of MQW- Al_2O_3 , whereas these are red-shifted in MQW-Si. These indicate GaN on MQW- Al_2O_3 experiences a compressive strain, and a tensile strain for MQW-Si.

TABLE I. Lattice constants and defect density calculated from the XRD and AFM data.

Samples	a (Å)	c (Å)	Strain (%)	(002) ω -FWHM (arcsec)	(102) ω -FWHM (arcsec)	D_{screw} (10^8 cm^{-2})	D_{edge} (10^8 cm^{-2})	TD density (10^8 cm^{-2})
MQW- Al_2O_3	3.1819	5.1929	+0.128	195.1	293.6	0.77	1.73	2.87
MQW-Si	3.1911	5.1819	-0.162	386.2	573.1	3.00	6.60	3.20

TABLE II. Strain and stress of the GaN buffer layers calculated from the Raman spectroscopy data.

Samples	E_2^H (cm ⁻¹)	$\Delta\omega$ (cm ⁻¹)	Stress (GPa)	Strain (%)
MQW-Al ₂ O ₃	569.7	2.2	0.512	+0.107
MQW-Si	565.7	-1.8	-0.419	-0.088
GaN (relaxed)	567.5			

$$D_{edge} = \frac{\beta_{(102)}^2 - \beta_{(002)}^2}{4.35 \times b_{edge}^2} \quad (5)$$

The results are tabulated in Table II, which shows MQW-Si contains approximately four times more screw- and edge-type dislocations than MQW-Al₂O₃.

Raman spectroscopy is conducted with a Horiba Confocal Raman Microscope with an 1800 l/mm grating and a $\lambda = 532$ nm laser using a Z(XX)Z configuration to calculate strain in the GaN layers of the InGa_{0.5}N MQW. As shown in Fig. 4b, MQW-Al₂O₃ shows three distinct Raman shifts: 417 cm⁻¹, which is attributed to the A_{1g} phonon mode from the Al₂O₃ substrate,¹⁴ and 569.7 and 735.3 cm⁻¹, which are associated with the E₂^H and A₁(LO) phonons of GaN.^{15,16} MQW-Si shows four Raman shifts: a saturated peak at 520 cm⁻¹ from the Si substrate, 565.7 and 732.1 cm⁻¹ from the E₂^H and A₁(LO) phonons of GaN, and a weak 646 cm⁻¹ peak, which is likely a E₂^H phonon mode associated with a AlGa_{0.5}N buffer layer.¹⁷ The E₂^H and A₁(LO) Raman shifts of GaN in the MQW-Al₂O₃ exhibits a blue-shift in energy from its relaxed value (567.5 cm⁻¹, 734.0 cm⁻¹, respectively); this indicates a compressive strain experienced in the GaN layer. MQW-Si exhibits the opposite shifts, which indicates the presence of a tensile strain. The E₂^H peak is used to calculate the stress based on its deviation from the relaxed value due to its high strain sensitivity.¹⁸ The in-plane biaxial stress is then calculated using:¹⁹

$$\Delta\omega = 4.3\sigma_{xx} \text{ cm}^{-1} \text{ GPa}^{-1}, \quad (6)$$

where $\Delta\omega$ is the Raman shift and σ_{xx} is the stress. The in-plane strain is calculated using:²⁰

$$\varepsilon_{xx} = \sigma_{xx} / [(C_{11} + C_{12}) - 2C_{13}^2 / C_{33}], \quad (7)$$

where C_{ij} are the elastic constants of GaN ($C_{11} = 390$ GPa, $C_{12} = 145$ GPa, $C_{13} = 106$ GPa, and $C_{33} = 398$ GPa),²¹ which give a proportionality factor of 478 GPa. The calculated in-plane stress and strain values are tabulated in Table II. Raman spectroscopy shows a compressive strain (-0.107%) in MQW-Al₂O₃ and tensile strain (+0.088%) in MQW-Si, in line with XRD results.

Figure 5 shows the PL spectra of (a) MQW-Al₂O₃ and (b) MQW-Si from 6 ~ 300 K obtained using a 10-mW frequency-tripled laser ($\lambda = 266$ nm) and a helium-bath cryostat, and the extracted temperature dependent (c) internal quantum efficiency (IQE) and (d) peak emission energy. MQW-Al₂O₃ exhibits InGa_{0.5}N multiple quantum well peak (MQW) centered at 2.812 eV at 300 K. At low temperature ($T < 100$ K), a shoulder on the low-energy (2.728 eV) side of the MQW peak and

a peak in the ultraviolet range (3.486 eV) appear. The low energy peak is attributed to the localized indium clusters,²² which is caused by the phase separation as a result of lattice mismatch,²³ whereas the UV peak is attributed to near-band-edge (NBE) emission from excitons recombining in the GaN layer.²⁴ The PL spectra for MQW-Si show three major emission centers: the MQW at 2.853 eV, donor-acceptor-pair (DAP) transition of GaN at 3.288 eV,²⁴ and NBE emissions from GaN at 3.446 eV. These emissions are convolved with the Fabry-Perot interference caused by the thinner films on the silicon substrate. The DAP emission exhibits the commonly seen LO-phonon replicas that are spaced at 90 meV apart.²⁵ The DAP recombination indicates the elevated impurity concentration in MQW-Si, while the stronger GaN NBE emission suggests the carrier confinement is poorer due to the lower crystal quality.

The difference of ~41 meV in the main MQW emissions from the samples throughout the temperature range (Fig. 5d), despite the same physical structure shown by XRD, is attributed to the reduced Quantum Confined Stark Effect (QCSE) in the InGa_{0.5}N active layers. The compressive strain experienced by the GaN layer in the MQW-Al₂O₃ leads to an even larger compressive strain in the InGa_{0.5}N wells. This leads to a stronger piezoelectric polarization field in the InGa_{0.5}N layer, and thus a reduction in the QW ground state energies. The tensile strain in the GaN layer of the MQW-Si leads to a reduced compressive strain in the InGa_{0.5}N layer, which in turn exhibits a reduced piezoelectric polarization.²⁶ The reduced QCSE is believed to increase the electron-hole wavefunction overlap, which should increase the efficiency of radiative recombination.

Figure 5c shows the temperature-dependent IQE, which is calculated using the following:

$$\text{IQE}(T) = \frac{I(T)}{I(6 \text{ K})}, \quad (8)$$

where $I(T)$ is the integrated intensity of the PL emission at temperature T , and assuming at 6 K all the recombination mechanisms are radiative. The IQE of the LEDs are shown in Fig. 5c. MQW-Si shows a steady decrease in IQE as the temperature increases, whereas Al₂O₃ exhibits a dip in IQE at 100 K. At room temperature, the IQE of the MQW-Al₂O₃ and MQW-Si are very similar at 33 and 30%, respectively, despite the difference in crystal quality observed by AFM and XRD. In fact, the IQE of MQW-Si exceeds that of MQW-Al₂O₃ at all temperatures below 250 K. This indicates that the activation energy of their respective carrier loss mechanism, either band filling or nonradiative recombination centers, are significantly different. This can be evaluated via Arrhenius activation energy analysis using:²⁷

$$I = \frac{I_0}{1 + C \exp(-E_{act}/kT)}, \quad (9)$$

where I is the integrated intensity, I_0 and C are fitting constants, k is the Boltzmann's constant, T is temperature, and E_{act} is the activation energy. This yields a E_{act} of 17 ± 3 meV for MQW-Al₂O₃ and 45 ± 4 meV for MQW-Si. This analysis

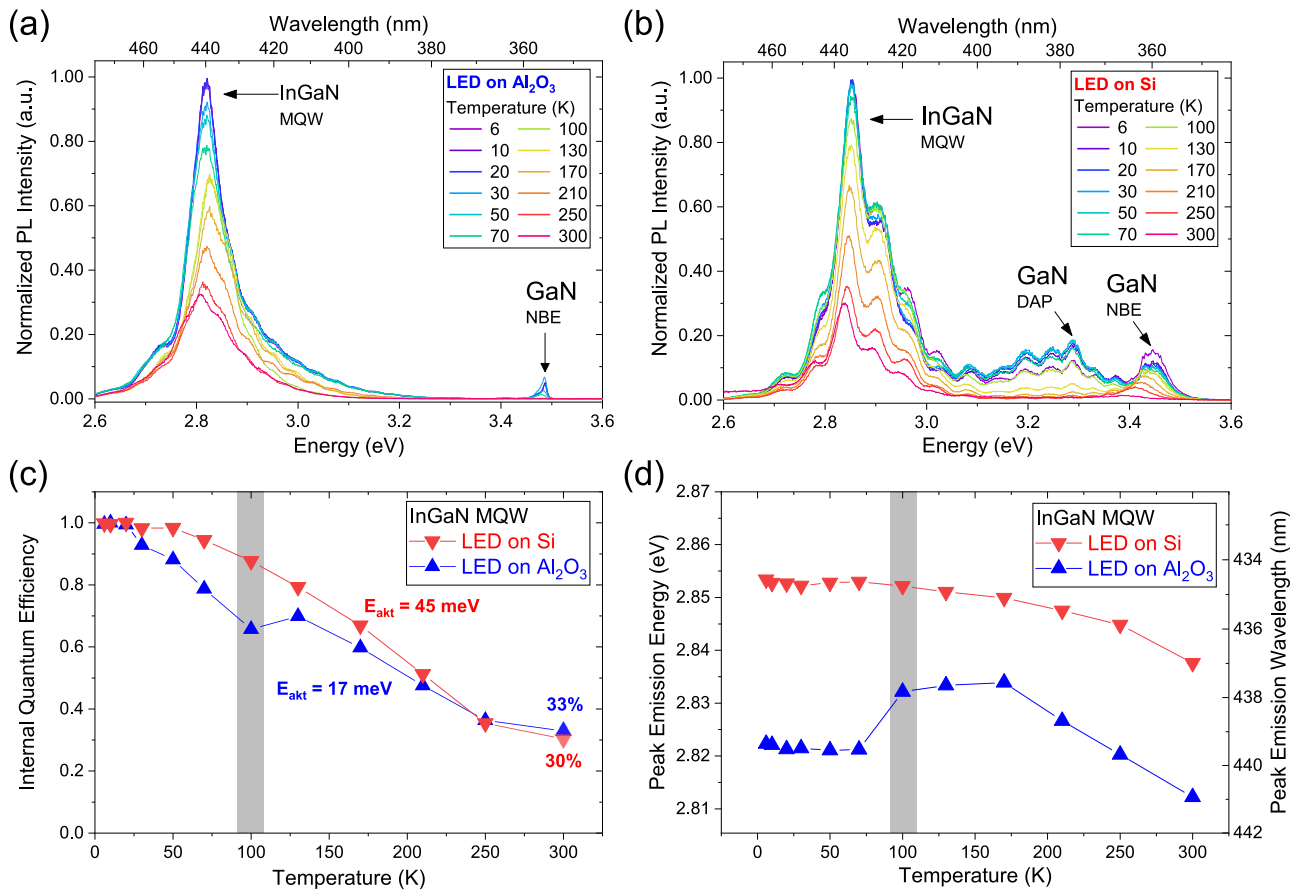


FIG. 5. Temperature dependent PL spectra of (a) MQW-Al₂O₃ and (b) MQW-Si from 6 K (purple) to 300 K (red). MQW-Si shows more carrier recombination via NBE and DAP in GaN. (c) Temperature-dependent IQE of (red) MQW-Si and (blue) MQW-Al₂O₃. The two samples exhibit similar IQE at 300 K. However, MQW-Si exhibits a higher IQE at temperature below 250 K. Arrhenius activation energy is calculated to be 17 meV (45 meV) for MQW-Al₂O₃ (on Si). (d) Temperature-dependent peak emission energy of (blue) MQW-Al₂O₃ and (red) on Si. While MQW-Si's peak emission red-shifts monotonically with increasing temperature due to the bandgap shrinkage, MQW-Al₂O₃'s peak emission exhibits a S-curve. An increase in IQE of MQW-Al₂O₃ with increasing temperature at 100 K coincides with a blue shift in the peak emission energy.

shows that the carriers in the local energy minima of MQW-Al₂O₃ requires very little thermal energy to escape to other higher energy emission centers, while MQW-Si requires 2.6 times more energy to activate a carrier loss mechanism.

The peak MQW emission energies from 6 to 300 K are plotted in Fig. 5d. The MQW emission from the MQW-Al₂O₃ exhibits a distinct S-shape shift in peak energy with increasing temperature in addition to the overall bandgap shrinkage, which is described by the Varshni coefficient.²⁸ The peak energy remains stable between 6 and 100 K, but then rapidly blue-shifts by 10 meV at 100 K, and then red-shifts by 21 meV steadily from 170 to 300 K. The S-shaped peak shift has been reported in the literature as caused by the temperature-dependent carrier dynamics in the self-organized inhomogeneous InGaN local minima.²⁹ The coincidence of a blue shift in the peak energy and an increase in the IQE of the MQW of the MQW-Al₂O₃ at 130 K suggests a change in the emission center as carriers gain enough thermal energy to freely move between the low energy minima and the higher energy minima

as the temperature increases.³⁰ On the other hand, the MQW emission from MQW-Si monotonically red-shifts by 16 meV with increasing temperature. To verify the reduced QCSE and the higher density of states in MQW-Si, power dependent PL is conducted.

Figure 6 shows the injection power dependent PL of (a) MQW-Al₂O₃ and (b) MQW-Si with laser power varying from 0.1 to 10 mW at 6 K. With 0.1 mW of laser power (purple spectrum), MQW-Al₂O₃ shows a main LED peak at 2.813 eV, a red shoulder at 2.755 eV, and a broad, undefined blue shoulder, whereas MQW-Si shows a main LED peak at 2.830 eV. A power-law dependence of the PL peak intensities on the laser power is fitted to quantify the difference between the two LEDs:³¹

$$I \propto P^m, \quad (10)$$

where I is the intensity of the emission, P is the power of the incident laser, and m is the power dependence. The fitting yields power dependence of 0.73 ± 0.04 (MQW-Al₂O₃ main peak), 0.75 ± 0.04 (MQW-Al₂O₃ red shoulder), and

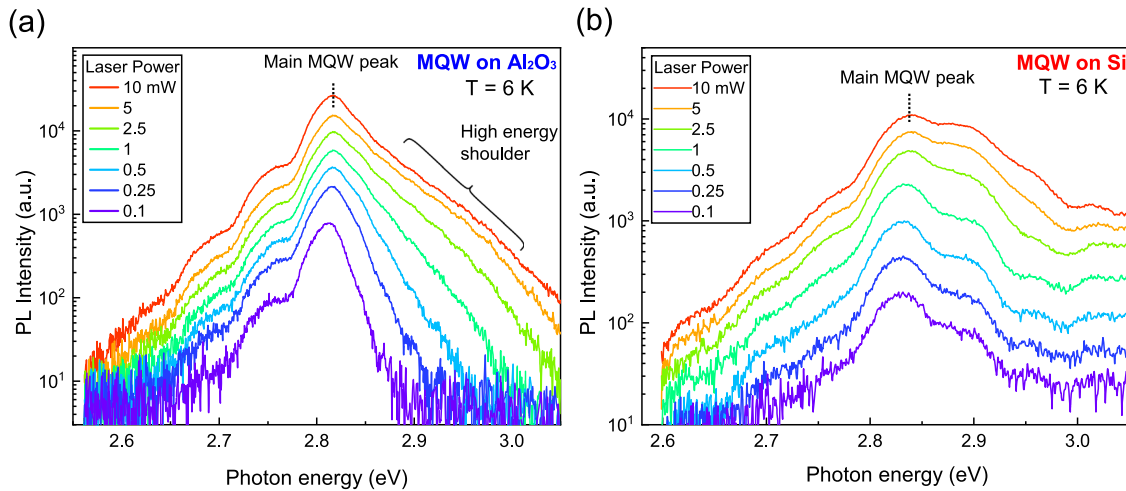


FIG. 6. Injection power-dependent photoluminescence at 6 K with laser power from 0.1 to 10 mW. (a) MQW-Al₂O₃ shows a sublinear relationship (0.73 ± 0.04) with injection laser power and an indistinct blue shoulder (b) MQW-Si shows a linear relationship (0.91 ± 0.05) behavior with laser power.

0.91 ± 0.05 (MQW-Si main peak). The sublinear power dependence observed in both emission centers for MQW-Al₂O₃ indicates the band filling of the low energy minima. This happens when a high concentration of injected carriers occupies all the available states in the lowest emission center, causing some of the carriers to occupy a otherwise higher energy states and subsequently emit photons with higher energies. The high energy shoulder has been reported to be a combination of the filling of the band-tail states and the screening of the internal electric fields.^{8,9}

The power-law fitting of the MQW-Al₂O₃ main peak is separated into two laser power regimes of 0.1 ~ 0.5 mW and 0.5 ~ 10 mW and the power dependences are $m = 0.94 \pm 0.09$ and $m = 0.65 \pm 0.02$, respectively. This shows that the main peak of MQW-Al₂O₃ exhibits a band-to-band-like transition that at laser power below 0.5 mW, whereas at laser power above 0.5 mW it exhibits defect-like band-filling behavior with a featureless high energy shoulder. MQW-Si, on the other hand, shows an approximately linear ($m \approx 1$) power dependence. The observed in MQW-Al₂O₃ is not present in MQW-Si. This suggests the bands in the main emission centers of MQW-Si are not fully-filled, and therefore the carrier spilling to higher energy states is not as pronounced. To observe the carrier recombination mechanisms in the MQW time-resolved photoluminescence (TRPL) is conducted.

Figure 7 shows the TRPL spectra and mono-exponential decay fit of TRPL spectra and mono-exponential decay fit of (solid blue) MQW-Al₂O₃ and (dashed red) MQW-Si. MQW-Al₂O₃ (blue) and MQW-Si (red) using a frequency-doubled Ti-Al₂O₃ laser ($\lambda = 380$ nm) to directly create electron-hole-pairs in the quantum well, and an avalanche photodiode with a bandpass filter to observe the LED emission. Using single exponential decay fitting, the PL lifetime of MQW-Al₂O₃ and MQW-Si are calculated to be 4.9 ± 0.3 and 7.3 ± 0.1 ns, respectively. Given the relationship of lifetimes with IQE³²

$$IQE = \frac{\tau_{rad}^{-1}}{\tau_{PL}^{-1}}, \quad (11)$$

where τ_{rad} and τ_{PL} are the radiative and photoluminescence lifetimes, the radiative lifetimes are calculated. Nonradiative recombination lifetimes (τ_{nr}) are calculated via

$$\tau_{PL}^{-1} = \tau_{rad}^{-1} + \tau_{nr}^{-1}. \quad (12)$$

Radiative (nonradiative) recombination lifetimes of 14.8 ns (7.3 ns) are calculated for the MQW-Al₂O₃ and 24.3 ns (10.4 ns)

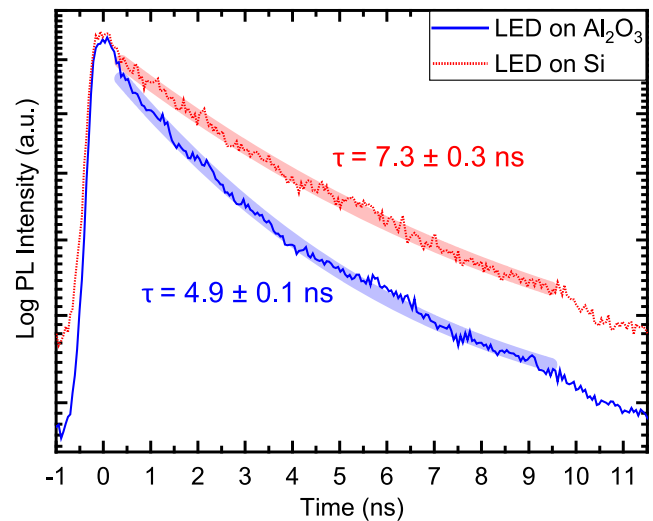


FIG. 7. Time-resolved photoluminescence of (blue solid) MQW-Al₂O₃ and (red dashed) MQW-Si using a frequency-doubled Ti:Sapphire laser at 390 nm to directly generate electron-hole-pairs in the InGaN quantum wells. Exponential decay fitting in the highlighted regions yields PL lifetimes of 7.3 ± 0.3 ns for MQW-Si and 4.9 ± 0.1 ns for MQW-Al₂O₃.

for MQW-Si. The faster radiative lifetime in MQW-Al₂O₃ is attributed to the higher carrier concentration in the smaller indium clusters, while the faster nonradiative lifetime is attributed to the carrier escape from these local potential minima. On the other hand, the slower radiative lifetime in MQW-Si suggests the recombination centers are operating in a lower carrier concentration regime, which has a lower probability of carrier escape. The net result of a reduced carrier escape probability and a lower crystal quality is a $\sim 40\%$ longer nonradiative lifetime.

III. DISCUSSION

It has been shown that the carrier dynamics are very different in MQW-Al₂O₃ and MQW-Si with the latter exhibiting less structural and optical characteristics that are associated with indium clustering. These include: S-shaped temperature-dependent PL peak emission energy, defect-like injection intensity dependence of the PL peaks, and correlation between intensity and spectral non-uniformities. The suppressed indium clustering effects are attributed to the residual tensile strain ($-0.088\% \sim -0.162\%$) in the GaN epitaxial layer in MQW-Si. It has been reported in the literature that tensile strain is beneficial for indium atom incorporation during MOCVD growth in the InGa_N MQW by strain compensation³³ and the increased indium incorporation.³⁴ The higher InGa_N uniformity indicates the ability of MQW-Si to incorporate a higher indium mole fraction than MQW-Al₂O₃ before phase separation becomes significant. This implies the possibility of achieving a higher indium content green InGa_N LED using the MQW-Si platform. Additionally, the tensile strain in the GaN layer can help reduce the compressive in the In_{0.15}Ga_{0.85}N layers and thus the piezoelectric polarization field. The reduced overall polarization field in the InGa_N layers is beneficial for high efficiency emitters via the greater electron-hole wavefunctions overlap.³⁵ Thus, for InGa_N devices on Si it may be more beneficial to not eliminate all the tensile strain originated from the silicon substrate in order to compensate for the compressive strain in the active InGa_N layers.

IV. CONCLUSION

In conclusion, MQW-Si is found to be superior to MQW-Al₂O₃ in emission wavelength and intensity areal uniformity, higher carrier loss mechanism activation energy, and the suppression of band-filling effect, as the result of a more uniform indium incorporation. This is attributed to the residual tensile strain found in the GaN layer of MQW-Si that also reduces the QCSE in the InGa_N layers. Despite a lower crystal quality, MQW-Si exhibits a higher IQE at temperatures below 250 K and a similar one at room temperature with an epitaxial thickness that is 30% thinner. Overall, the results presented herein demonstrates the advantages of growing blue InGa_N/GaN MQW emitters on Si over Al₂O₃ substrates.

ACKNOWLEDGMENTS

This work is supported by the National Science Foundation Faculty Early Career Development (CAREER) Program

under award number NSF-ECCS-16-52871. R. Liu acknowledges support from the NASA Space Technology Research Fellowship (NSTRF-1). C. McCormick acknowledges support by the National Science Foundation Faculty Early Career Development (CAREER) Program under award number NSF ECCS 16-52871 CAR REU. This work was carried out in the Micro and Nanotechnology Laboratory and Frederick Seitz Materials Research Laboratory Central Research Facilities, University of Illinois at Urbana-Champaign, IL, USA. The authors acknowledge the support from Dr. Mauro Sardela and Dr. Julio Soares from the University of Illinois at Urbana-Champaign, IL, USA.

REFERENCES

- E. Schmitt, T. Straubinger, M. Rasp, and A. D. Weber, *Superlattices Microstruct.* **40**, 320 (2006).
- D. Zhu, D. J. Wallis, and C. J. Humphreys, *Rep. Prog. Phys.* **76**, 106501 (2013).
- M. Lee, M. Yang, K. M. Song, and S. Park, *ACS Photonics* **5**, 1453 (2018).
- H.-P. Lee, J. Perozek, L. D. Rosario, and C. Bayram, *Sci. Rep.* **6**, 37588 (2016).
- A. Dadgar, T. Hempel, J. Bläsing, O. Schulz, S. Fritze, J. Christen, and A. Krost, *Phys. Status Solidi Curr. Top. Solid State Phys.* **8**, 1503 (2011).
- J.-Y. Kim, Y. Tak, J. Kim, H.-G. Hong, S. Chae, J. W. Lee, H. Choi, Y. Park, U.-I. Chung, J.-R. Kim, and J.-I. Shim, *Proc. SPIE* **8262**, 82621D (2012).
- H. Y. Ryu, K. S. Jeon, M. G. Kang, H. K. Yuh, Y. H. Choi, and J. S. Lee, *Sci. Rep.* **7**, 44814 (2017).
- K. Kazlauskas, G. Tamulaitis, J. Mickevicius, E. Kuokstis, A. Žukauskas, Y.-C. C. Cheng, H.-C. C. Wang, C.-F. F. Huang, and C. C. Yang, *J. Appl. Phys.* **97**, 013525 (2005).
- Y. J. Lee, C. H. Chiu, C. C. Ke, P. C. Lin, T. C. Lu, H. C. Kuo, and S. C. Wang, *IEEE J. Sel. Top. Quantum Electron.* **15**, 1137 (2009).
- B. Heying, E. J. Tarsa, C. R. Elsass, P. Fini, S. P. DenBaars, and J. S. Speck, *J. Appl. Phys.* **85**, 6470 (1999).
- M. A. Moram and M. E. Vickers, *Reports Prog. Phys.* **72**, 036502 (2009).
- A. Kadir, C. C. Huang, K. E. Kian Lee, E. A. Fitzgerald, and S. J. Chua, *Appl. Phys. Lett.* **105**, 232113 (2014).
- B.-T. Liou, S.-H. Yen, and Y.-K. Kuo, *Proc. SPIE* **5628**, 296 (2005).
- S. P. S. Porto and R. S. Krishnan, *J. Chem. Phys.* **47**, 1009 (1967).
- H. Harima, *J. Phys. Condens. Matter* **14**, R967 (2002).
- V. Y. Davydov, Y. E. Kitaev, I. Goncharuk, A. Smirnov, J. Graul, O. Semchinova, and D. Uffmann, *Phys. Rev. B - Condens. Matter Mater. Phys.* **58**, 12899 (1998).
- M. Kuball, *Surf. Interface Anal.* **31**, 987 (2001).
- F. Demangeot, J. Frandon, M. A. Renucci, O. Briot, B. Gil, and R. L. Aulombard, *Solid State Commun* **100**, 207 (1996).
- S. Tripathy, S. J. Chua, P. Chen, and Z. L. Miao, *J. Appl. Phys.* **92**, 3503 (2002).
- J. Gleize, F. Demangeot, J. Frandon, M. A. Renucci, F. Widmann, and B. Daudin, *Appl. Phys. Lett.* **74**, 703 (1999).
- A. Polian, M. Grimsditch, and I. Grzegory, *J. Appl. Phys.* **79**, 3343 (1996).
- S. Chichibu, K. Wada, and S. Nakamura, *Appl. Phys. Lett.* **71**, 2346 (1997).
- Y.-S. Lin, K.-J. Ma, C. Hsu, S.-W. Feng, Y.-C. Cheng, C.-C. Liao, C. C. Yang, C.-C. Chou, C.-M. Lee, and J.-I. Chyi, *Appl. Phys. Lett.* **77**, 2988 (2000).
- M. A. Reshchikov, M. Zafar Iqbal, S. S. Park, K. Y. Lee, D. Tsvetkov, V. Dmitriev, and H. Morkoç, *Phys. B Condens. Matter*, 444-447 (2003).
- T. Azuhata, T. Sota, K. Suzuki, and S. Nakamura, *J. Phys. Condens. Matter* **7**, L129 (1995).
- J.-H. Ryou, P. Douglas Yoder, J. Liu, Z. Lochner, H. Kim, H. Jin Kim, and R. D. Dupuis, *IEEE J. Sel. Top. Quantum Electron.* **15**(4), 1080 (2009).

- ²⁷J. Krustok, H. Collan, and K. Hjelt, *J. Appl. Phys.* **81**, 1442 (1997).
- ²⁸Y. P. Varshni, *Physica* **34**, 149 (1967).
- ²⁹Y. Cho, G. H. Gainer, A. J. Fischer, J. J. Song, S. Keller, U. K. Mishra, and S. P. DenBaars, *Appl. Phys. Lett.* **73**, 1370 (1998).
- ³⁰Z. Wang, L. Wang, Y. Xing, D. Yang, J. Yu, Z. Hao, C. Sun, B. Xiong, Y. Han, J. Wang, H. Li, and Y. Luo, *ACS Photonics* **4**, 2078 (2017).
- ³¹W. Grieshaber, E. F. Schubert, I. D. Goepfert, R. F. Karlicek, M. J. Schurman, and C. Tran, *J. Appl. Phys.* **80**, 4615 (1996).
- ³²Y. Narukawa, Y. Kawakami, S. Fujita, and S. Nakamura, *Phys. Rev. B* **59**, 10283 (1999).
- ³³S.-H. Park, Y.-T. Moon, J. S. Lee, H. K. Kwon, J. S. Park, and D. Ahn, *Phys. Status Solidi* **208**, 195 (2011).
- ³⁴M. C. Johnson, E. D. Bourret-Courchesne, J. Wu, Z. Liliental-Weber, D. N. Zakharov, R. J. Jorgenson, T. B. Ng, D. E. McCready, and J. R. Williams, *J. Appl. Phys.* **96**, 1381 (2004).
- ³⁵M. Monavarian, A. Rashidi, A. A. Aragon, M. Nami, S. H. Oh, S. P. Denbaars, and D. Feezell, *Appl. Phys. Lett.* **112**, 191102 (2018).